TEM characterization of advanced kesterite structures

Author: Robert Fonoll Rubio
Facultat de Física, Universitat de Barcelona, Diagonal 645, 08028 Barcelona, Spain.

Advisors: Sònia Estradé Albiol, Víctor Izquierdo Roca and Javier Blanco Portals

Abstract **– In the present work, we study a kesterite $Cu_2ZnSnSe_4$ solar cell at the nanoscale level in order to analyze the defects that lower its energy conversion efficiency. First of all, current density–voltage characteristics, quantum efficiency, photoluminiscence, and Raman spectroscopy are studied to obtain macroscopic and microscopic information about the device. Then, High Resolution Transmission Electron Microscopy (HRTEM) is performed to observe the cross-section and, for the first time, the front interface of the absorber with nanoscopic detail.**

Index Terms **– 5. Nanostructured materials: HRTEM, Kesterite, Solar cell, Transmission Electron Microscopy**

I. INTRODUCTION

Kesterite $Cu_2ZnSn(S_xSe_{1-x})_4$ (CZTSSe) is a promising absorber photovoltaic (PV) material. Currently, silicon is the most used material for fabricating solar cells, representing 96% of PV production in 2016 [1]. It has achieved a laboratory energy conversion efficiency (E_{ff}) of 26% [2], but it is reaching its theoretical limit. An alternative to silicon are chalcopyrite $Cu(In_{1-x}Ga_x)Se_2$ (CIGS) thin film solar cells, that have achieved efficiencies as high as 22.6% [3] and present the advantages of a higher absorption coefficient thanks to the direct optical band gap, and a better matching with the solar spectrum thanks to the possibility of tunning this band gap [1]. However, it contains critical raw materials like indium and gallium. So, kesterite family of compounds, which has the advantages of CIGS with the additional one of being composed of non-toxic and earth abundant elements, could be the best option for fabricating solar cells.

CZTSSe has achieved a cell efficiency of 12.6% [4]. Despite having a lower performance than Si and CIGS-based solar cells, kesterite family has been investigated for a much shorter time, so further investigation could make it to outperform the other materials. Taking this into account, solving the current limitations of kesterite is fundamental. These limitations include band gap fluctuations, poor collection at all wavelengths, short carrier lifetime, and high series resistance, among others [5].

Kesterite has been studied by almost all available macroscopic characterization techniques, but very little research has been done at the nanoscopic level. So, in order to study the causes of the above mentioned problems, we use High Resolution Transmission Electron Microscopy (HRTEM) to observe the $Cu_2ZnSnSe_4$ (CZTSe) structure and to characterize it. We use TEM because it offers the best range of characterization techniques with the highest resolution. It consists in transmitting a small beam of high-energy electrons through an extremely thin sample. The interaction between the electrons and the periodic potential in a given crystal generates an image which allows us to observe features such as the crystal structure or the density of defects at the nanoscale [6].

A. Kesterite: $Cu_2ZnSnSe_4$

Cu_2ZnSnS_4 (CZTS) was identified as a possible absorber PV material in 1988, and the first CZTS solar cell was fabricated in 1996 [1]. Since then, its efficiency has been improved by trying different materials and deposition techniques, and the current certified record efficiency is 12.6%, reported by Mitzi group at IBM in a CTZSSe cell [4].

Kesterite can be synthesized by different techniques, that, in general, can be classified in two groups. The first one are the vacuum-based deposition techniques like thermal evaporation, sputtering, pulsed laser deposition (PLD), or other physical vapor deposition (PVD) techniques. The second one are the non-vacuum deposition techniques like solution processing, chemical synthesis of a nanoparticle solution, or electrochemical deposition. Hydrazinebased solution approach is the one that has given the current highest efficiency, but both groups of deposition techniques are currently producing similar results.

On the positive side, the main advantages of kesterite are: it is composed of non-toxic and earth abundant elements, it has p-type conductivity, it has a higher absorption coefficient ($\sim 10^4 cm^{-1}$ [7]) thanks to its direct band gap, the band gap can be tuned by changing the S/Se ratio (from 1.0 eV for pure CZTSe to 1.5 eV for pure CZTS [8]) and with cation substitution, and it is compatible with the well-known CIGS technology [1].

However, kesterite still presents some limitations to be solved before starting its industrialization. The main reported problems for this material are short minority carrier lifetime, front interface recombination, grain boundary recombination, band gap fluctuations, high series resistance, electrostatic potential fluctuations, insufficient quasi-fermi level splitting, and bias dependent photocurrent. These problems can be caused by Shockley-

TABLE I: Energy conversion efficiency (E_{ff}), open-circuit voltage (V_{oc}), short-circuit current (J_{sc}), and fill factor (FF) of the CZTSe, CZTS, and CZTSSe record solar cell devices.

Material	E_{ff} (%)	V_{OC} (mV)	J_{SC} (mA/cm^2)	FF (%)
CZTSe[9]	11.6	423	40.6	67.3
CZTS[10]	9.2	708	21.6	60.0
CZTSSe[4]	12.6	513	35.2	69.8

Read-Hall recombination on point defects, tunneling assited recombination, non-radiative carrier recombination, absorber decomposition at the front interface, high density of non-passivated surface defects, a poor charge inversion in the absorber, existance of too small grains, poor grain boundary passivation, presence of secondary phases in the bulk, Cu/Zn disorder, voids at the back interface, and small diffusion length in the absorber, among others [5]. Finally, these defects cause open-circuit voltage (V_{OC}), short-circuit current (J_{SC}), and fill factor (FF) losses, which, at their turn, reduce the solar cell efficiency. So, solving the causes of these limitations is fundamental to take kesterite solar cells to mass production

In this work, we study a high-efficiency CZTSe solar cell ($E_{ff} = 9.2\%$). The reason to work with CZTSe compounds is that they have achieved a higher efficiency than CZTS and a similar one that CZTSSe, as can be seen in Table I. Furthermore, CZTSe is technologically simpler than CZTSSe since it is composed of less elements. So, CZTSe is the most promising of the compounds of the kesterite family for achiving mass production.

Since carrier recombination has an important role in energy conversion efficiency loss, HRTEM study can help to improve the CZTSe solar cell performance by identifying the causes of this problem like non-passivated surface defects.

Regarding its crystal structure, kesterite has a tetragonal crystal lattice and its $A^I_2B^{II}C^{IV}X^{VI}_4$ compounds are distributed as following: each anion X^{VI} is surrounded by two A^I, one B^{II}, and one C^{IV}, and every cation is tetrahedrally coordinated by X^{VI}, as can be seen in Fig. 1.a [1]. This structure can suffer extended defects such as stacking faults (SF) and antisite domain boundaries (ADB), which are shown in Fig. 1.b-e. The stacking sequences of intrinsic SFs are (...ABC/BC/ABC...) and the ones of extrinsic SFs are (...ABC/ABAC/ABC...), thus generating a supercell having a SF. SFs increase the band gap, so they act as an electron barrier and make electron extraction difficult. ADBs are represented by cation disorder, producing higher formation energy and lower band gap, thus acting as recombination centers [11].

B. Objectives

The main objective of this work is to study a high-efficiency $Cu_2ZnSnSe_4$ solar cell ($E_{ff} = 9.2\%$ without antireflective coating nor contacts) at the nanoscopic level by HRTEM in order to perform a deep characterization of the potential defects that cause limitations in the performance of the kesterite.

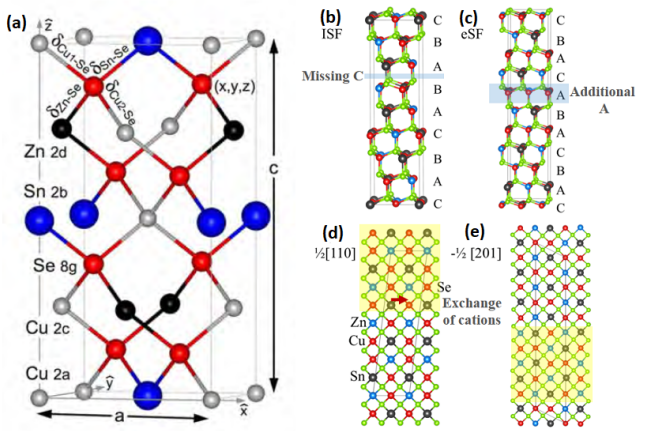

FIG. 1: (a) Conventional unit cell of kesterite CZTSe [1]. Atomic structure of (b) intrinsic stacking faults, (c) extrinsic stacking fault in kesterite, and antisite domain boundaries with the fault displacement of (d) $\frac{1}{2}$ [110] or (e) $-\frac{1}{2}$ [201]. Solid lines represent the boundaries of the supercells [11].

On the one hand, cross-section TEM study is performed to observe grain boundaries and defects in the bulk of the grains. On the other hand, we also aim to develop for the first time (according to our knowledge) a methodology based in planar-view geomtry that will allow the characterization at the nanoscale of the front interface between the CZTSe absorber and the CdS buffer layer, which is a critical interface.

Specially, we want to identify defects that cause carrier recombination like the existence of too small grains, a poor grain boundary passivation, band gap narrowing, the presence of minor phases at front interface due to absorber decomposition, a Fermi level pinning, a poor charge inversion in the absorber, a high density of non-passivated surface defects at the front interface, and point defects in the bulk.

Furthermore, current density–voltage (J–V) characteristic, quatum efficiency (QE), photoluminescence (PL), and Raman spectroscopy are used to study the optoelectronical and optical characteristics of the sample.

II. METHODOLOGY

In this work, we have studied a high-efficiency CZTSe absorber sample (Fig. 2). It was synthesized at IREC by the group of Solar Energy Materials and Systems. DC magnetron sputtering was used to deposite Cu/Sn/Cu/Zn metallic stacks with an additional 10 nm Ge nanolayer onto a Mo coated soda lime glass substrate, all of this under a Se + Sn atmosphere. Thin films were derived with Cu-poor and Zn-rich compositions due to

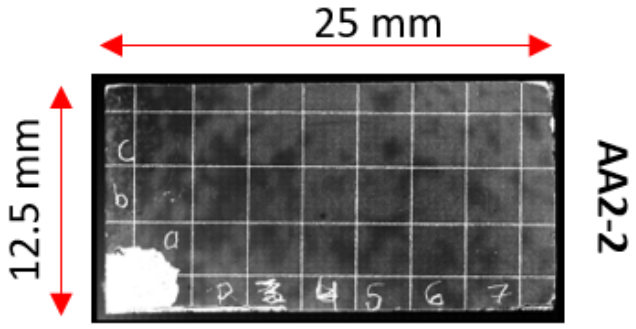

FIG. 2: Image of the studied kesterite-based solar cell device.

detrimental intrinsic defects like Sn_{Zn} and $2Cu_{Zn}$+Sn_{Zn} in the stoichiometric compositions, with composition ratios of $\frac{[Cu]}{[Zn]+[Sn]} = 0.73$ and $\frac{[Zn]}{[Sn]} = 1.11$. The deposition was followed by a reactive annealing process and, later, by several etching processes to remove secondary phases and to passivate the surface. Finally, a CdS buffer layer was deposited by chemical bath deposition, followed by pulsed DC magnetron sputtering deposition of ZnO and In_2O_3-Sn_2O (ITO) window layer.

We characterized the sample by the following techniques.

A. Optoelectronical characterization

For each cell of the device, we performed current density (J)–voltage (V) measurements while the device was under an ABET3000 Solar Simulator with AM1.5 conditions.

Then, we obtained the quantum efficiency using a PV300 Photovoltaic characterization system (Bentham Instruments).

On the one hand, the external quantum efficiency (EQE) indicates the quantity of carriers that are generated by each incident photon at each wavelength. Ideally, since carriers are generated by photons with energies higher than the band gap, the solar cell should have 100% of EQE at wavelengths lower than the one corresponding to the band gap energy, and 0% of EQE at wavelengths higher than that.

On the other hand, the internal quantum efficiency (IQE) is the quantity of carriers that are generated by each photon that has reached the absorber at each wavelength. In other words, IQE is the quantum efficiency obtained when ignoring the reflected photons, the sum of EQE and the reflectance.

Once we have the EQE curve, we can estimate the band gap (E_g) of our sample using its inflection point near the absorption edge, which corresponds to the minimum of the first derivative of the EQE.

B. Optical characterization

Raman scattering measurements were performed in back scattering configuration with a LabRam HR800-UV Horiba-Jobin Yvon system.

Raman spectroscopy is based on inelastic scattering of monochromatic light by the sample. It consists in irradiating the sample with a laser beam and, then, the absorbed photons are reemitted with a different frequency. Raman peaks provides information about the vibrationa modes of the material, and their intensity and position depend on the material composition, the crystalline defects and the doping. Specially, the use of UV-resonant condition enhances the sensitivity.

In addition, we obtained the PL spectrum using a iHR320 Horiba-Jobin Yvon system. PL measures the light emitted by the material after the absorption of photons. We can also estimate E_g by looking at which energy this spectrum presents its maximum, since the maximum emission is produced where the maximum absorption has taken place.

C. HRTEM characterization

TEM samples are prepared to get electron transparent specimens, which means having samples of 30-50 nm in thickness, with 100 nm as an upper limit.

For the cross-section TEM observation, samples were prepared by focused ion beam (FIB).

For the planar-view observation, first of all, the CZTSe sample was cut with a diamond saw into pieces around 1 x 3 mm. These pieces were polished with a series of diamond abrasive films with decreasing grain sizes of 30, 15, 6, 1, and 0.5 μm until 30 - 70 μm thickness was reached. The final thinning was done by ion milling using Precision Ion Polishing System (PIPS) with the upper source working at 5.0 kV and 5.0 mA. The main difficulties presented during planar-view sample preparation are that the CZTSe sample is too thick, so it is difficult to achieve electron transparent thickness and the observable area is small; and, since it is a granular sample, CZTSe can loss its structure during polishing or ion milling due to loss of grains.

After the preparation, planar-view images were acquired in a J2100 with a LaB_6 gun at 200 keV, and cross-section images in a J2010F at 200 keV. Once we had the set of TEM and HRTEM images, we used Gatan DigitalMicrograph software to analyze them. We also used CaRIne Crystallography software to identify the atomic planes of Fast Fourier Transform (FFT) and difraction patterns. The parameters for building the crystal structure of CZTSe were obtained from the Inorganic Material Database (AtomWork).

TEM is based on electron scattering. When the beam of electrons pass through the sample, some electrons remain undeviated and some are scattered by a set of planes

of atoms due to Couloumb interactions, resulting on a non-uniform distribution that contains the information about the sample. Using a restricting aperture or an electron detector that only selects electrons with a certain angle of deviation, we can choose which electrons form the image and thus we control the information that it presents. Bright field (BF) images are obtained using direct beams, while dark field (DF) images are obtained using diffracted beams [6].

Electron scattering is elastic if there is no loss of energy and it is inelastic if there is a considerable loss of energy. The first case is the major source of contrast and intensity in TEM images. Electrons that are scattered elastically through small angles (less than 3°) are coherent, which means that they have a phase relationship.This scattering is referred to as diffraction, which involves treating the electron as a wave and is the most significant phenomenon in the TEM.

In order to explain the diffraction process, we will considere atoms that are stacked together regularly in a crystal structure. In real space, we can define any lattice vector, $\mathbf{r}_n$, by the equation:

$$\mathbf{r}_n = n_1\mathbf{a} + n_2\mathbf{b} + n_3\mathbf{c} \tag{1}$$

where the vectors **a**, **b** and **c** are the unit-cell translations in real space and are called the primitive vectors. n_1, n_2 and n_3 are all integers.

We introduce here the concept of the reciprocal lattice, which represents the Fourier transform of another lattice. So, it is a lattice in reciprocal space and is a purely geometrical construction. Any reciprocal-lattice vector, **G**, can be defined as following:

$$\mathbf{G} = h\mathbf{a}^* + k\mathbf{b}^* + l\mathbf{c}^* \tag{2}$$

where h, k and l are integers that define the plane (hkl). The definition of this plane is that it cuts the a, b and c axes at $1/h, 1/k$ and $1/l$, respectively. Another important concept is the zone axis (ZA), which is a lattice row parallel to the intersection of two or more families of lattices planes. Moreover, $\mathbf{a}^*, \mathbf{b}^*$ and $\mathbf{c}^*$ are the primitive vectors in reciprocal space and can be expressed as

$$\mathbf{a}^* = \frac{2\pi(\mathbf{b}\wedge\mathbf{c})}{\mathbf{a}\cdot(\mathbf{b}\wedge\mathbf{c})}; \mathbf{b}^* = \frac{2\pi(\mathbf{c}\wedge\mathbf{a})}{\mathbf{a}\cdot(\mathbf{b}\wedge\mathbf{c})}; \mathbf{c}^* = \frac{2\pi(\mathbf{a}\wedge\mathbf{b})}{\mathbf{a}\cdot(\mathbf{b}\wedge\mathbf{c})} \tag{3}$$

In the reciprocal lattice, sets of parallel (hkl) atomic planes are represented by a single point located a distance $1/d_{hkl}$ from the lattice origin [6]. d_{hkl} is the interplanar spacing:

$$d_{hkl} = \frac{1}{|\mathbf{G}|} \tag{4}$$

Therefore, if an object or a length is large in real space, then it is small in reciprocal space.

The basic property of a crystal is that its inner potential, V (**r**), is periodic and positive. This property is expressed by

$$V(\mathbf{r}) = V(\mathbf{r} + \mathbf{R}) \tag{5}$$

where **R** represents any lattice vector of the crystal and ***r*** represents any real-space vector. Since it is periodic, we can express it as a Fourier series in which we sum over all the lattice points in reciprocal space

$$V(\mathbf{r}) = \sum_G V_{\mathbf{G}} e^{i\mathbf{G}\cdot\mathbf{r}} \tag{6}$$

being $V_{\mathbf{G}}$ the Fourier coefficient, which is the **G** component of V in the series.

Due to this periodic potential, an electron in a crystal can be described by the sum of Bloch waves

$$\psi_k(\mathbf{r}) = u_k(\mathbf{r}) \cdot e^{i\mathbf{k}\cdot\mathbf{r}} \tag{7}$$

where $u_k(\mathbf{r})$ is a periodic function and **k** is a wave vector of a plane wave.

We introduce now the structure factor F(θ), which is a measure of the amplitude of an electron wave scattered by a unit cell of a crystal structure, and it has dimensions of length. We can define F(θ) as the sum of the f(θ) terms from all the i atoms in the unit cell multiplied by a phase factor f_i. The phase factor takes account of the difference in phase between waves scattered from atoms on different but parallel atomic planes with the same Miller indices (hkl). The scattering angle (θ) is the angle between the incident and scattered electron beams. It gives us the following expression:

$$F(\theta) = \sum_i^\infty f_i e^{-2\pi i(hx_i + ky_i + lz_i)} \tag{8}$$

In consequence, the amplitude of scattering depends on the type of atom ($f(\theta)$), the position of the atom in the cell (x, y, z), and the specific atomic planes (hkl) that make up the crystal structure. Furthermore, $|F(\theta)|^2$ is proportional to the scattered intensity, which determines the contrast of the TEM images. This equation predicts that in certain circumstances the amplitude of scattering is zero, which is called a systematic absence and is very useful to do a diagnostic test when determining crystal structures in the TEM.

Finally, the positions of the diffracted beams are determined by the size and shape of the unit cell. The diffraction process from a TEM specimen is described by the Bragg's Law:

$$n\lambda = 2dsin\theta \tag{9}$$

where d is the distance between two reflecting hkl planes and θ is the incident angle of the wave. We can see that atomic planes which are closer together give rise to larger angles of scatter, a very important aspect in diffraction-pattern interpretation. So, by choosing λ for the incident electron (which we control with the accelerating voltage) and measuring θ experimentally, we can find the interplanar spacings in our sample.

The mode of the TEM that we use is the HRTEM, which maximizes the useful detail in the image. The

beam passing through the lens at high spatial frequenciess is bent through a larger angle by the objective lens, so each point in the sample plane is transformed into an extended region in the final image and, in consequence, each point in the final image has contributions from many points in the sample. Here, we need to apply the weak phase-object approximation (WPOA), which says that, for a very thin sample, the amplitude of a transmitted wave function depends linearly on the projected potential of the sample.

The image formation can be mathematically expressed as convolution of the point-spread function, *h(r)*, and the function that describes the points of the specimen, *f(r)*:

$$g(\mathbf{r}) = \int f(\mathbf{r}')h(\mathbf{r}-\mathbf{r}')d\mathbf{r}' = f(\mathbf{r}) \otimes h(\mathbf{r}-\mathbf{r}') \qquad (10)$$

The convolution is a complicated operation in real space, but it is a simple multiplication in reciprocal space. By performing Fourier transforms, we obtain the functions in reciprocal space. The Fourier transform is expressed by:

$$F(\omega) = \int_{-\infty}^{+\infty} f(x)e^{i\omega x}d\omega \qquad (11)$$

So, the Fourier transform of Eq. 10 is:

$$G(\mathbf{u}) = H(\mathbf{u}) \cdot F(\mathbf{u}) \qquad (12)$$

Thus, in this work we are going to use the Fast Fourier Transform (FFT), a fast algorithm for computing the discrete Fourier Transform. The FFT computes the Fourier transform in $O(NlogN)$ operations, instead of the $O(N^2)$ operations needed without this algorithm, where N is the number of points of the discrete function [12].

Furthermore, another configuration that we use is scanning transmission electron microscopy (STEM), where the microscope lenses are adjusted to create a focused convergent electron beam at the sample surface. This focused beam is scanned across the sample and various signals are collected point-by-point to form an image. Its advantages over TEM is that it enables the use of other signals that cannot be spatially correlated in TEM, including secondary electrons, scattered beam electrons, characteristic X-rays, and electron energy loss. Its advantage over SEM is the improvement in spatial resolution.

III. RESULTS AND DISCUSSION

A. Macroscopic characterization

First of all, from the J(V) curves of each device of the characterized sample showed in Fig. 2, we have obtained the data shown in Fig 3. Our device has a mean energy conversion efficiency of 8.6% and a maximum one of 9.4%, and mean values of J_{SC} = 28.0 mA/cm^2, V_{OC} = 453.0 mV, and FF = 67.7%, all of this without antireflective coating. We can compare these values to the ones of the record CTZSe device that are shown in Table I and are represented in Fig. 4.a. Although E_{ff} is lower, the use of antireflective coating and electrical contacts could produce a similar efficiency around 11%, so we are working with a sample that, currently, offers one of the best performances among CZTSe solar cells. However, we can see in the same Fig. 4.a that our cell needs to be improved in order to achieve the efficiency of the record CISe solar cell (E_{ff} = 15.0%[13]) and, furthermore, all parameters have lower values in comparision with Shockley–Queisser limit [14], which can be explained by the limitations of the material presented in Section I.A.

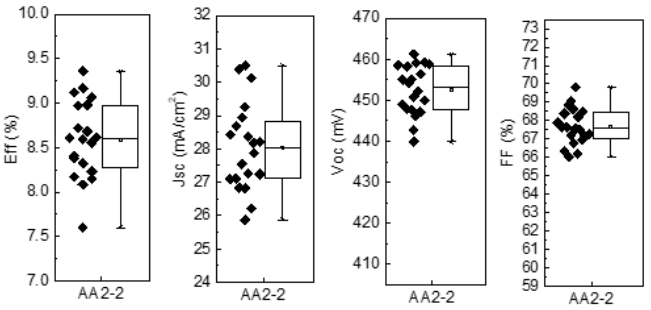

FIG. 3: Energy conversion efficiency (Eff), short-circuit current (Jsc), open-circuit voltage (Voc), and fill factor (FF) of a CZTSe solar cell devices. Each point corresponds to the value of each cell of the device, the rectangle indicates the mean value and its error, and the bar indicates the maximum and minimum value obtained from each sample.

In Fig. 4.b, we have the EQE/IQE spectra of the device of our cell with higher E_{ff}, whose J(V) curve is shown in Fig. 4.a. These spectra indicate efficiency losses due to reflection and due to photon absorption in the ITO ($E_g \approx$ 4.0 eV), ZnO (E_g = 3.4 eV) and CdS (E_g = 2.4 eV) layers. And even if they reach the absorber, photons with energies in the near infrared region are weakly absorbed and can be transmitted. Finally, the generated carriers might not be collected if the collection length, which is the sum of the space charge width and the diffusion length, is shorter than the absorber thickness [15].

The band gap of our kesterite obtained from EQE is 1.031 eV, and the one obtained from PL is 0.983 eV. The difference of 0.048 eV between the two obtained E_g can be explained by the fact that PL gives the minimum energy for photons to be absorbed (optical band gap), while EQE gives the minimum energy for generating an electron–hole pair that is not bound together (electrical or transport band gap). However, the large difference between the EQE band gap, PL signal and the broad PL full width half maximum indicate the presence of band gap fluctuations.

According to the Shockley–Queisser limit, at E_g = 1.031 eV, the energy conversion eficiency of 9.4% of our cell represents around 30% of its theoretical limit, so there is room for improvement.

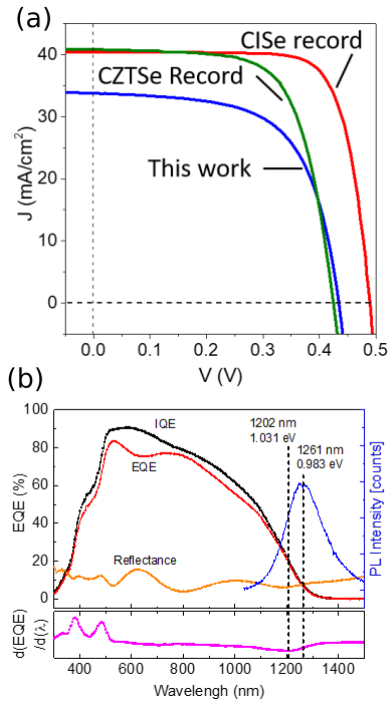

FIG. 4: (a) J–V curve of the sample studied in this work (blue), the CZTSe record solar cell (green) and the CISe record solar cell (red). (b) Internal and external quantum efficiency (IQE and EQE), reflectivity, photoluminescence (PL), and first derivative of the EQE spectra of a CZTSe solar cell. Dashed lines indicate the band gap obtained from the EQE and the PL spectra.

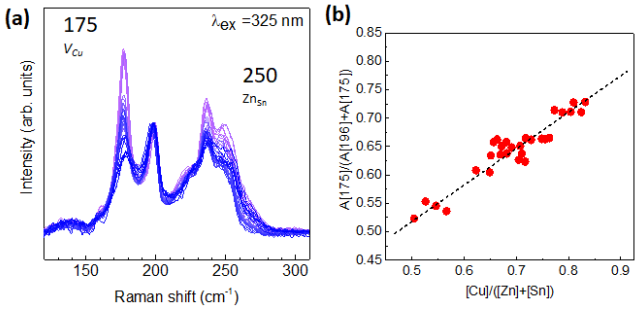

FIG. 5: (a) Raman spectrum of a CZTSe solar cell measured in UV-resonant condition. (b) Relationship between the [Cu]/([Zn]+[Sn]) ratio and the area under the 175 cm^{-1} Raman peak.

The Raman spectrum at UV-resonant condition (excitation wavelength of 325 nm) is shown in Fig. 5.a, where the observed peaks agree with theoretical predictions [16]. Fig. 5.b indicates that the intensity of the 175 cm^{-1} Raman peak decreases as the Cu concentration in CZTSe decreases. According to that, the variations of the 175 cm^{-1} peak in the UV Raman mapping shown in Fig. 6.a are related to the presence of copper vacancies (V_{Cu}) defects (peak intensity decreases with the increase of this defect), while the variations of the 250 cm^{-1} peak

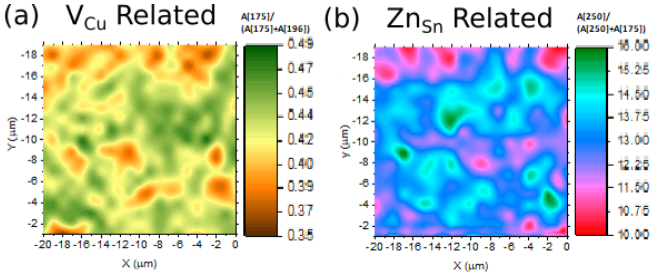

FIG. 6: UV Raman mapping of a 20 μm x 20 μm region of a kesterite solar cell indicating the variations of the area under the (a) 175 cm^{-1} peak and (b) 250 cm^{-1} peak.

in Fig. 6.b indicate the presence of zinc on tin antisites (Zn_{Sn}). These defects are recombination centers that lower the efficiency of the device, and their presence indicate inhomogeneity in the composition at microscopic level.

B. TEM results: cross-section geometry

If we look at Fig. 7, we have a collage of cross-section images (each one being as de-magnified as possible in STEM mode) to show the whole structure of CZTSe and the rest of the layers. The brightest areas of the bright field (BF) images (or the darkest ones of the dark field images) correspond to voids at the back interface, which produce high series resistance since carriers have to travel a longer path, thus lowering the FF of the solar cell. We can see that these voids are only present in this back interface between the CZTSe absorber and the $MoSe_2$ back electrode, they are not seen in the bulk of the absorber nor in the front interface. In addition, it is worth to note that contrast differences in the bulk of the absorber are due to thickness differences, diffraction effects and artifacts produced when making the collage.

In Fig. 8, we can see the bulk of the absorber with high resolution. We observe well-defined grain boundaries that are narrow and regular, without any remarkable defect. In addition, the performed Fast Fourier Transforms (FFT) show the same [021] zone axis (ZA) for three different grains of the sample, although the patterns are rotated with respect to each other. This indicates a shared orientation along the CZTSe layer, being the common axis the one parallel to the direction of observation (this is, perpendicular to the cross-section observed). The rotation in the FFT patterns translates into an equal rotation between the grains along the zone axis. These rotations imply that there is no single orientation along the vertical direction of the absorber, which is the direction along which the carriers move. In consequence, carriers have to change their path and this facilitates their recombination.

In Fig. 9.a, another region of the bulk of the absorber is observed. Grain boundaries are again regular and nar-

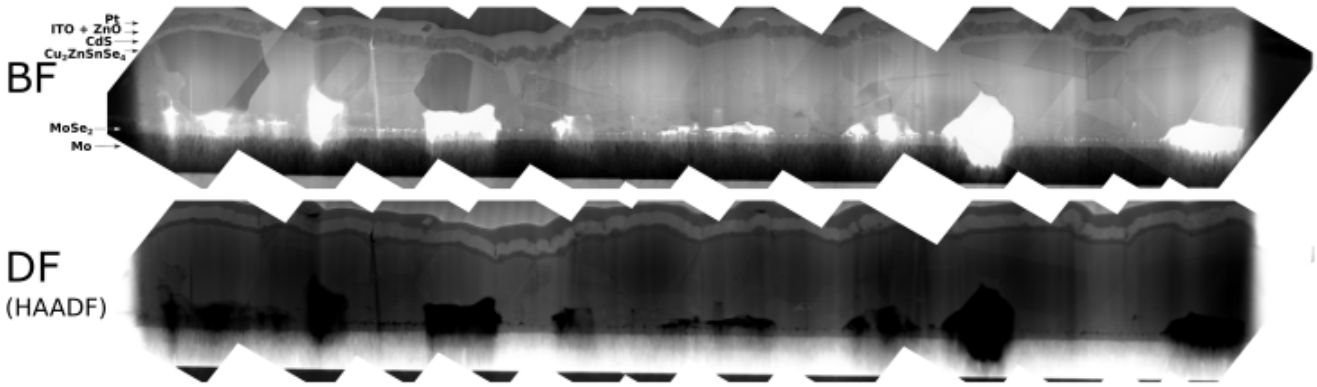

FIG. 7: Collage image of a series of bright field (BF) and dark field (DF) images (high angular annular dark field, HAADF, images).

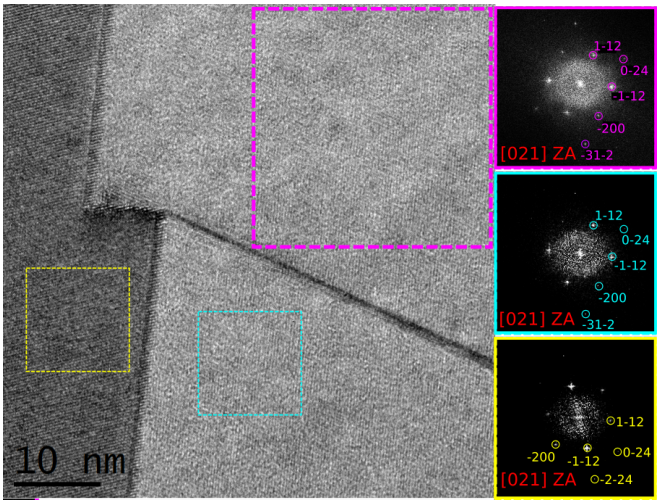

FIG. 8: Cross-section HRTEM image of boundaries between three CZTSe grains at the bulk of the absorber and the Fast Fourier Transform (FFT) of the selected areas with the dashed rectangles.

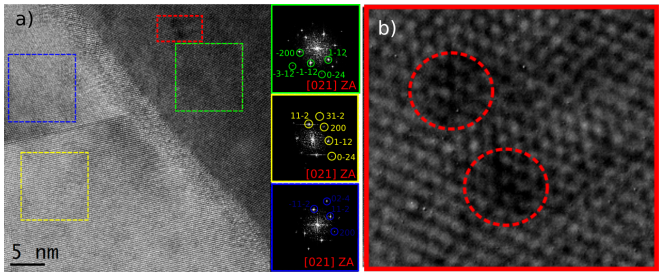

FIG. 9: (a) Cross-section HRTEM image of boundaries between three CZTSe grains at the bulk of the absorber and FFT of the selected areas with the dashed rectangles (green, yellow, and blue insets). (b) Zoomed HRTEM image of the area indicated with the dashed red rectangle in (a).

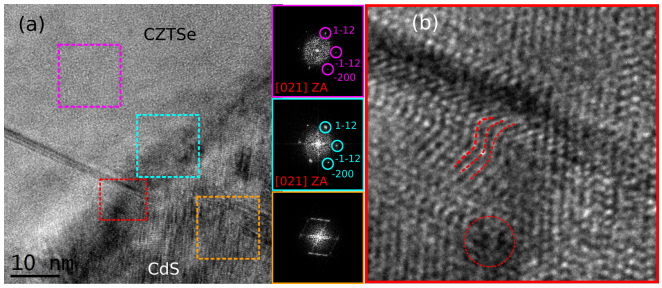

FIG. 10: (a) Cross-section HRTEM image of the front interface between CZTSe absorber and the CdS layer, and FFT of the selected areas with the dashed rectangles (purple, cyan, and orange insets). (b) Zoomed HRTEM image of the area indicated with the dashed red rectangle in (a).

row (some apparent difference is due to height differences between the grains). FFTs show again a [021] ZA with rotated patterns, which confirms the shared orientation along the direction perpendicular to the cross-section observed. In addition, we can see in Fig. 9.b some point defects indicated with red, dashed circles. These point defects in the bulk are Shockley-Read-Hall recombination centers that reduce the carriers lifetime and cause V_{OC} loss.

In Fig. 10.a, we can observe the front interface of the absorber. At some nanometers from the interface, FFT of the CZTSe grain have the same [021] ZA. However, CdS layer produce a deformed FFT due to the high density of defects in its structure. And just at the interface between the two materials, we can identify the first nanometers of the absorber by the FFT with the same [021] ZA as the others CZTSe grains (region selected with the dashed cyan rectangle). However, in these first nanometers of the absorber (between 5 and 15 nm) we can observe a high density of defects, as can be seen in Fig. 10.b, where we have indicated with red lines some observed dislocations

and we have also indicated some point defects with a red circle. This is an important difference with respect to the well-defined grain boundaries in the bulk. We can suppose that these defects are produced by a strain in this front interface.

C. TEM results: planar-view geometry

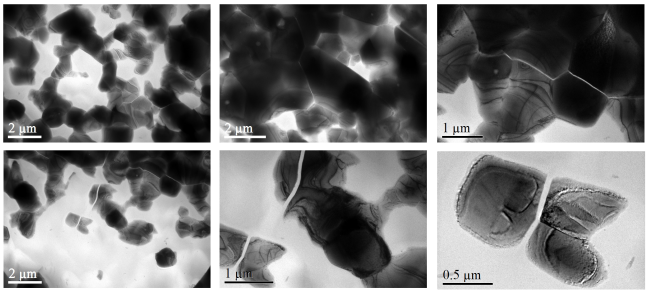

FIG. 11: Set of planar-view TEM images at different magnifications of the front interface of a CZTSe sample.

In the planar-view TEM images of Fig. 11, we can see different regions at different magnifications of the front interface of the CZTSe absorber. We can distinguish some grains delimited by bright boundaries that are regular and narrow, so no remarkable defects are observed in the grain boundaries at these magnifications in planar-view geometry. It is worth to note that the brighter areas corresponding to empty areas are produced during the ion milling, they are not an intrinsic characteristic of the material.

In Fig. 12, we have indexated some difraction patterns obtained from the sample, which correspond to [1 11 -7], [332], and [24-1] ZA. Since they have different ZA, the grains from which they were obtained have different crystalline orientation along the direction perpendicular to the planar-view observed, in agreement with the results observed in the bulk under cross-section configuration characterization.

Now, looking at Fig. 13, we see the surface of a CZTSe

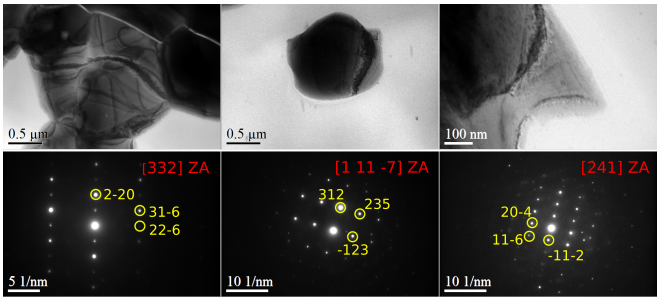

FIG. 12: Set of planar-view TEM images (top row) and the difraction patterns of the corresponding areas (bottom row) of a CZTSe sample.

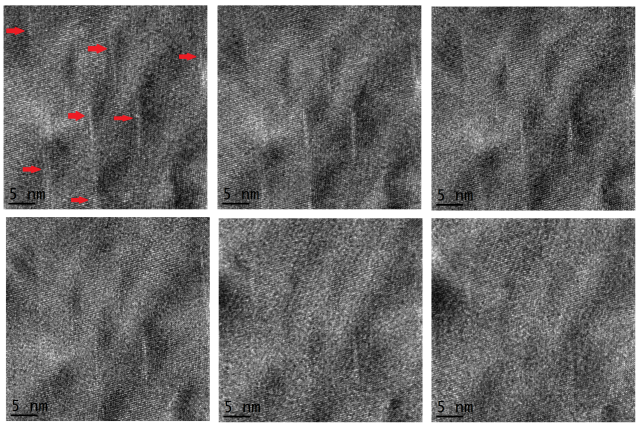

FIG. 13: Set of planar-view HRTEM images of the same area of the front interface of a CZTSe sample at different focus. The red arrows indicate the defects

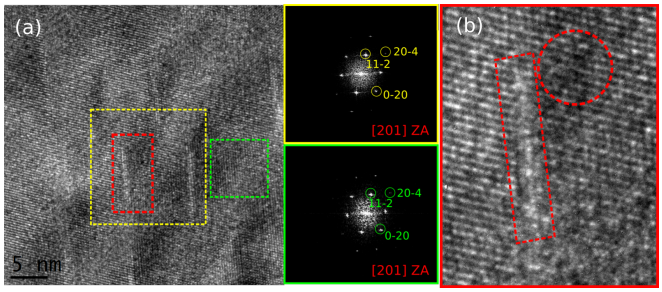

FIG. 14: (a) Planar-view HRTEM image of the front interface of a CZTSe absorber, and FFT of the selected areas with the dashed rectangles (yellow and green insets). (b) Zoomed HRTEM image of the area indicated with the dashed red rectangle in (a).

grain at the front interface with high resolution. Indicated with red arrows, we can see some short, narrow, white lines distributed over this surface, which are structural defects of the sample that could be stacking faults. We acquired images of the same area using different focus and, since the defects change with the focus, we can confirm that these defects are at a different height than the surrounding surface. Analyzing these defects, they have a length between 5 and 10 nm. Furthermore, they are distributed in groups that follow the same pathway, so these are periodic defects. This periodicity may indicate that they are due to stress relaxation. In Fig. 14.a, we have performed a FFT of the same front interface area that reveals a [201] ZA. The selected areas with defects (yellow) and without them (green) give the same pattern, indicating that these defects do not affect the planes orientation. In Fig. 14.b, we can have a close examination to one of these defects (indicated with a red dashed rectangle) and we can also see other surface defects that are indicated with a red circle. So, we can conclude that the front interface between the CZTSe absorber and the CdS layer have a high density of surface defects that produce

recombination in this interface, thus lowering the V_{OC}. It is the first time that these front interface defects have been reported in CZTSe.

IV. CONCLUSIONS

In conclusion, the cross-section HRTEM study of a CZTSe solar cell shows voids at the back interface of the absorber, which contribute to the FF loss. It also shows changes of crystal orientation along the vertical direction of the absorber, point defects in the bulk of the absorber, and a high density of defects in the front interface of the absorber in contrast with the good crystal quality observed in the bulk, all of which causes carrier recombination and lowers the V_{OC}.

In addition, it has been possible for the first time to perform a planar-view HRTEM study of the front interface of the CZTSe absorber. It shows a high density of surface defects that are recombination centers and that can explain the energy conversion efficiency losses.

In conclusion, further research of CZTSe solar cell should be aimed at avoiding the voids at the back interface and at improving the front interface in order to reduce the carrier recombination.

Acknowledgments

I would like to thank Sònia Estradé Albiol for her confidence in me and her teaching through all these years. I would like to thank Javier Blanco Portals for his patience in the numerous preparation and observation TEM sessions, and for the great knowledge he taught me. And I would like to thank Víctor Izquierdo Roca for opening the IREC doors for me and for introducing me in the world of photovoltaic technology. This project would not exists without the three of them.

Jacob Andrade, Lluís López, Catalina Coll, and Francesca Peiró also have played a fundamental role in this project and I thank them for that.

Finally, I want to thank my family and my friends for their support.

[1] Giraldo, S. Advanced strategies for high efficiency kesterite thin film solar cells. PhD thesis. Universitat de Barcelona, 2018.

[2] Green, M. A.; Hishikawa, Y.; Warta, W.; Dunlop, E. D.; Levi, D. H.; Hohl-Ebinger, J.; Ho-Baillie, A. W. H. Solar Cell Efficiency Tables (Version 50). *Prog. Photovoltaics Res. Appl.* **2017**, *25* (7), 668–676.

[3] Jackson, P.; Wuerz, R.; Hariskos, D.; Lotter, E.; Witte, W.; Powalla, M. Effects of Heavy Alkali Elements in Cu(In,Ga)Se2 Solar Cells with Efficiencies up to 22.6%. *Phys. Status Solidi - Rapid Res. Lett.* **2016**, *10* (8), 583–586.

[4] Wang, W.; Winkler, M. T.; Gunawan, O.; Gokmen, T.; Todorov, T. K.; Zhu, Y.; Mitzi, D. B. Device Characteristics of CZTSSe Thin-Film Solar Cells with 12.6% Efficiency. *Adv. Energy Mater.* **2014**, *4* (7), 1301465.

[5] Grenet, L.; Suzon, M. A. A.; Emieux, F.; Roux, F. Analysis of Failure Modes in Kesterite Solar Cells. *ACS Appl. Energy Mater.*, to be published.

[6] Williams, D. B. & Carter, C. B., *Transmission Electron Microscopy: A Textbook for Materials Science*, (Springer Science+Business Media, LLC, New York, 2009).

[7] Seol, J.; Lee, S.; Lee, J.; Nam, H.; Kim, K. Electrical and Optical Properties of CuZnSnS Thin Films Prepared by Rf Magnetron Sputtering Process. *Sol. Energy Mater. Sol. Cells* **2003**, *75* (12), 155–162.

[8] He, J.; Sun, L.; Chen, S.; Chen, Y.; Yang, P.; Chu, J. Composition Dependence of Structure and Optical Properties of Cu2ZnSn(S,Se)4 Solid Solutions: An Experimental Study. *J. Alloys Compd.* **2012**, *511* (1), 129–132.

[9] Lee, Y. S.; Gershon, T.; Gunawan, O.; Todorov, T. K.; Gokmen, T.; Virgus, Y.; Guha, S. $Cu_2ZnSnSe_4$ Thin-Film Solar Cells by Thermal Co-evaporation with 11.6% Eficiency and Improved Minority Carrier Diffusion Length. *Adv. Energy Mater.* **2015**, *5*, 1401372.

[10] Kato, T.; Hiroi, H.; Sakai, N.; Muraoka, S.; Sugimoto, H. Characterization of front and back interfaces on Cu_2ZnSnS_4 thin-film solar cells. Proceedings of 27th European Photovoltaic Solar Energy Conference, 2012, Frankfurt, Germany.

[11] Park, J.-S.; Kim, S.; Walsh, A. Opposing effects of stacking faults and antisite domain boundaries on the conduction band edge in kesterite quaternary semiconductors. *Phys. rev. Materials* **2018**, *2*, 014602.

[12] Press, W. H.; Teukolsky, S. A.; Vetterling, W. T.; Flannery, B. P., *Numerical Recipes in Fortran 77: The Art of Scientific Computing*, (Cambridge University Press, New York, 1992)

[13] AbuShama, J.; Noufi, R.; Johnston, S.; Ward, S.; Wu, X. Improved Performance in $CuInSe_2$ and Surface-Modified $CuGaSe_2$ Solar Cells. 31st IEEE Photovoltaics Specialists Conference and Exhibition, January 37, 2005, Lake Buena Vista, Florida.

[14] Shockley, W.; Queisser, H. J. Detailed Balance Limit of Efficiency of p-n Junction Solar Cells. *J. Appl. Phys.* **1961**, *32*, 510–519.

[15] Siebentritt, S. What limits the efficiency of chalcopyrite solar cells? *Sol. Energy Mater Sol. Cells.* **2011**, *95*, 1471–1476

[16] Gurel, T.; Sevik, C.; Cagin, T. Characterization of vibrational and mechanical properties of quaternary compounds Cu2ZnSnS4 and Cu2ZnSnSe4 in kesterite and stannite structures *Phys. Rev. B* **2011**, *84*, 205201